Common Carotid Artery Lumen Segmentation from Cardiac Cycle-resolved Cine Fast Spin Echo Magnetic Resonance Imaging

Lívia Rodrigues, Letícia Rittner, Roberto Lotufo
Faculty of Electrical and Computer Engineering
Medical Image Computing Lab
University of Campinas,Campinas, SP, Brazil
{lmarodr,lrittner,lotufo}@dca.fee.unicamp.br

Roberto Souza, Richard Frayne
Department of Radiology and Clinical Neuroscience
Hotchkiss Brain Institute
University of Calgary, Calgary, AB, Canada
{roberto.medeiros.deso,rfrayne}@ucalgary.ca

Abstract—**Atherosclerosis is a disease responsible for millions of deaths each year, primarily due to heart attack and stroke. Magnetic resonance (MR) imaging is a non-invasive method that can be used to analyze the carotid artery and detect signs of atherosclerosis. Most MR methods acquire high contrast, static images. These methods, however, are sensitive to artifacts from cardiac motion, produce time-averaged images, and do not allow for carotid distensibility analysis. Carotid distensibility is an important, systematic measure of vascular health. Cine fast spin echo (FSE) is a new MR imaging that can obtain dynamic MR data (*i.e.*, cardiac phase-resolved datasets). Dynamic imaging, however, comes at the cost of lower spatial resolution and signal-to-noise ratio, making these data potentially more difficult to segment. This paper introduces a semi-automated segmentation method that segments the common carotid artery (CCA) lumen across the cardiac cycle from dynamic MR images. To the best of our knowledge, this work is the first proposed technique for segmenting cardiac cycle-resolved cine FSE images. It combines *a priori* knowledge about the size and shape of the CCA, with the max-tree data structure, the tie-zone watershed transform (using identified internal and external markers) and supervised classification, to segment the carotid artery wall-lumen boundary. The user has to select only a seed point (centred in the carotid artery lumen). Technique performance was assessed using forty-five cine FSE data sets, each consisting of images reconstructed at sixteen temporal bins across the cardiac cycle. The automatic segmentation results were compared against the consensus of three different manual segmentation results. Our technique achieved an average Dice coefficient, sensitivity and false positive rate of 0.928 ± 0.031 (mean $\pm$ standard deviation), 0.915 ± 0.037 and 0.056 ± 0.049, respectively. Our method achieved higher agreement *versus* the consensus of the three manual segmentations than the individual manual segmentations *versus* the consensus.**

Index Terms—**max-tree, watershed transform, carotid artery imaging, carotid artery segmentation, carotid artery distensibility, cine FSE**

I. Introduction

Stroke is the most common cause of death in the world. It is estimated that 4.4 million people die every year due to stroke and 5,000 in every 1,000,000 people suffer from stroke-related disability [1]. Atherosclerosis is one of the main causes of ischemic stroke, causing about 25% of all events [2]. Atherosclerotic vessel disease is characterized by accumulation of lipid, fibrin, cholesterol and calcium in artery walls, specifically at bifurcations and in regions of vessel curvature. Atherosclerosis progression is complex with severe cases resulting in complex plaques in the vessel wall and, eventually, a reduction in cross-sectional area (*i.e.*, the development of lumenal stenosis).

In order to decrease the rate of ischemic stroke due to atherosclerosis, it is desirable to use a non-invasive method to quantify, monitor and assess carotid artery stenosis and plaque composition. Magnetic resonance (MR) imaging is a technique that permits the evaluation of morphology and composition. Using MR imaging, one can better define the absence or presence of vulnerable (or "at-risk") carotid plaques [1] that can be treated medically (*e.g.*, statin therapy) or with surgery. In order to evaluate the carotid morphology and composition, an important initial step is segmenting the carotid artery wall-lumen boundary. Most methods for segmenting the carotid artery were derived for use with computed tomography angiography images [3], but a few studies segment the carotid artery from static MR images. These approaches can be divided into three groups [4]:

- *Geometric models*, based on vessel shape. Some commonly used features include elongation, radius and bifurcation. Arias-Lorza et al. [5] use a centerline initialization followed by a surface graph cut algorithm. This method permits the localization of the inner and outer walls of the vessel in a semiautomatic way.
- *Appearance models*, based on luminance properties, depend on the imaging modality. Kumar et al. [6] creates an edge detection model based on the histogram equalization of the image and previous pre-processing.
- *Hybrid models*, combining appearance and geometric models. Sakellarios et al. [7] combine ellipse fitting for boundary detection and fuzzy clustering for lumen and plaque segmentation.

Despite the large amount of research, currently there are no public methods available for automatic or semi-automatic segmentation of carotid MR images, either static or dynamic.

In the present work, a hybrid model was used in cine fast spin echo (cine FSE) time-series of MR images with the initial goal of segmenting the common carotid artery (CCA) lumen. Our method uses the max-tree [8] area signature analysis combined with the tie-zone watershed transform from markers [9], [10] and supervised classification to get accurate segmentations. The user has to provide one marker for each of the left and right carotid arteries. The main contribution of this work is the development of a semi-automatic method to segment the lumen of CCA in cine FSE images. To the best of our knowledge this is the first work that tries to segment the CCA lumen using cine FSE images. This is important because it opens the possibility of assessing carotid artery distensibility, which is expected to be correlated with atherosclerotic disease.

This paper is organized as follows: Section II presents a brief theoretical background necessary to understand the method. Section III describes our method. Section IV presents the results and discussion. Finally, Section V presents the work conclusions and intended future work.

II. BACKGROUND

A. Cine FSE Images

Conventional static MR imaging techniques generate images with acceptable vessel wall-blood image contrast and allow for the depiction of vessel wall morphology and characterization of plaques components. FSE images, with proton density-, T1- and/or T2-weightings are commonly used [1], [2]. These images provide only a snap-shot (time averaged) of the vessel wall morphology and composition over the cardiac cycle. They can also suffer from cardiac motion-induced artifacts due to their long data acquisition times [11]. Cine FSE imaging is a new technique that is capable of acquiring images across the cardiac cycle in total acquisition times similar to those required for a standard static FSE technique, albeit often with reduced spatial resolution [11], [12]. Because cine FSE images are resolved over the cardiac cycle they potentially can reduce image artifacts due to motion [12].

Cine FSE acquires data over the entire acquisition window asynchronously with respect to the contraction of the heart. The acquired raw MR data is however tagged with its acquisition time within the cardiac cycle (typically using information from a pulse oximeter). The raw data is then rebinned into N temporal bins that evenly cover the average cardiac cycle. N is user selectable and typically is between 10 and 20. Because the raw MR data was collected asynchrounoulsy, each rebinned data set will, in general, be incomplete. Therefore sophisticated, non-linear reconstruction methods, based on compressed sensing [13], are required to generate images. Compared to static FSE images, cine FSE images are able to generate a similar range of image contrasts (weightings), with potentially lower resolution and signal-to-noise, but fewer motion artifacts. For this project, we used sequences of images rebinned into 16 temporal bins, as we can see on Figure 1. The cine FSE data acquisition process is fully explained in Boesen et al. [12].
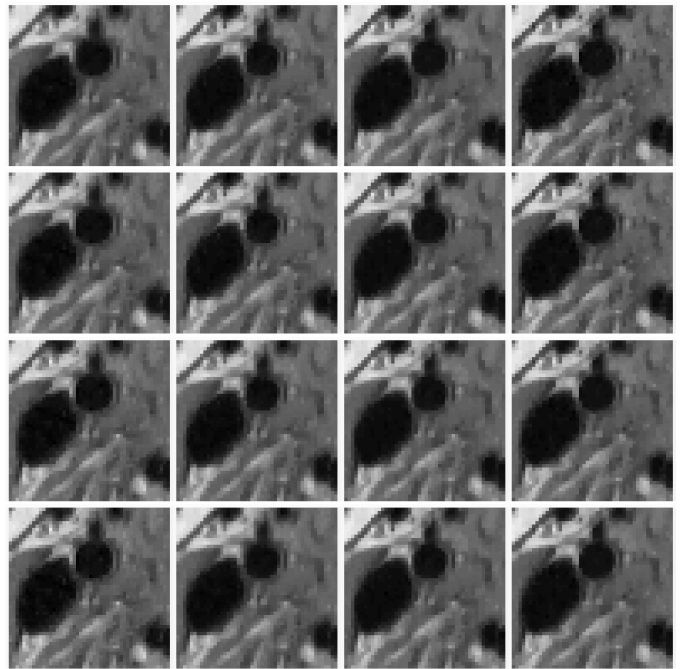

Fig. 1. Sequence of 16 temporal bins of the same slice during the cardiac cycle (zoom in around a CCA) collected with Cine FSE technique.

B. Max-tree

An upper threshold of a gray-scale image results in a binary image, where each pixel with a value greater or equal to the threshold receives the value 1 (white) and all other pixels receive value 0 (black). Loosely speaking, a binary image is composed of "islands", which in image processing are called connected components. The connected components have an inclusion relationship, the higher the threshold value the smaller the component will be. At increasingly larger thresholds, the component may even split in two or more components. The max-tree [8] represents an image through the hierarchical relationship of its connected components. Each node of the max-tree represents a different connected component resulting from an upper threshold. The leaves in the max-tree represent regional maxima in the image. If interested in processing minima, the duality property may be employed by processing the negative of the image. A simplified illustration of the max-tree corresponding to the negated slice of a carotid MR image is depicted in Figure 2.

Many size, shape and gray-level intensity attributes, such as area (or volume), bounding-box coordinates, circularity, average gray-level can be efficiently extracted from the max-tree nodes [14], to enable tasks like object recognition and segmentation [15].

C. Max-tree Signature Analysis

The max-tree signature consists of analyzing the variation of an attribute of any pair of nodes connected by a max-tree path. It conveys information concerning the variation in shape
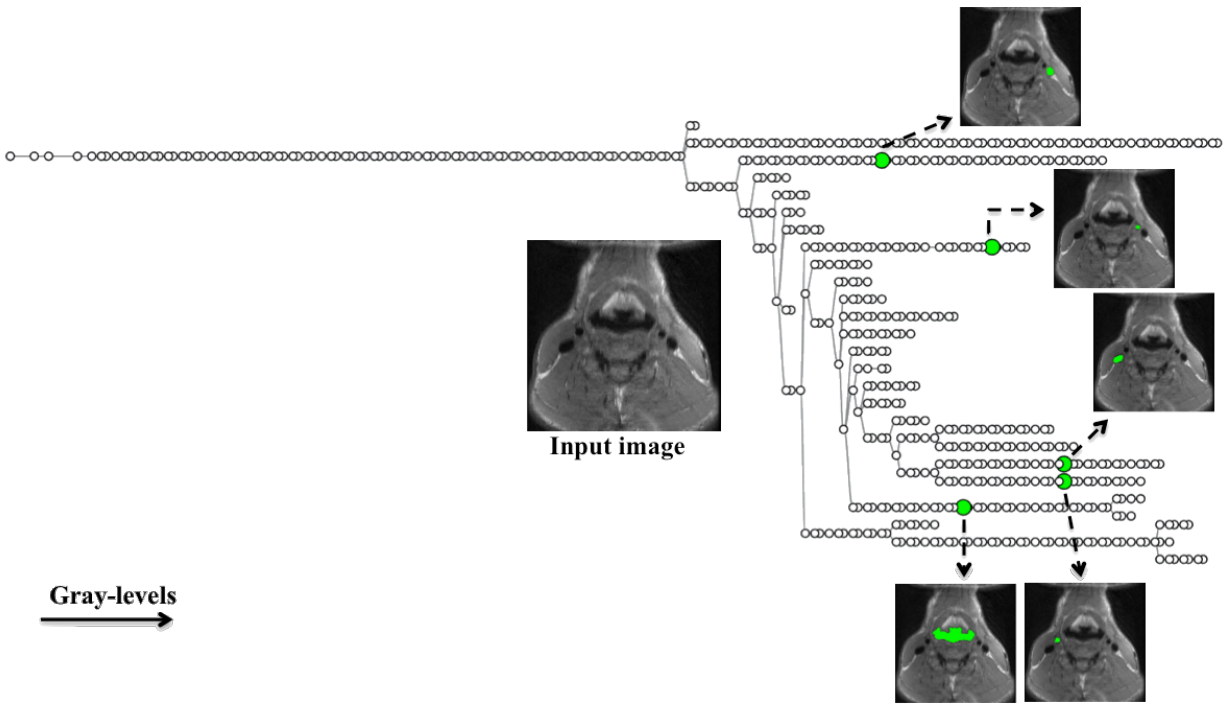
Fig. 2. Max-tree illustration of the negated input image. The arrows point to some of the connected components corresponding to the max-tree nodes (highlighted in green).

and/or size of a connected component. The attribute signature uses the linking information between connected components at sequential gray-levels in the image to help the decision making process. The area signature of the max-tree of the negative of the input image depicted in Figure 2 starting in a node inside the carotid (highlighted in green) and ending at the max-tree root is illustrated in Figure 3. We can see that for higher thresholds the carotid lumen starts to separate itself from the rest of the image.
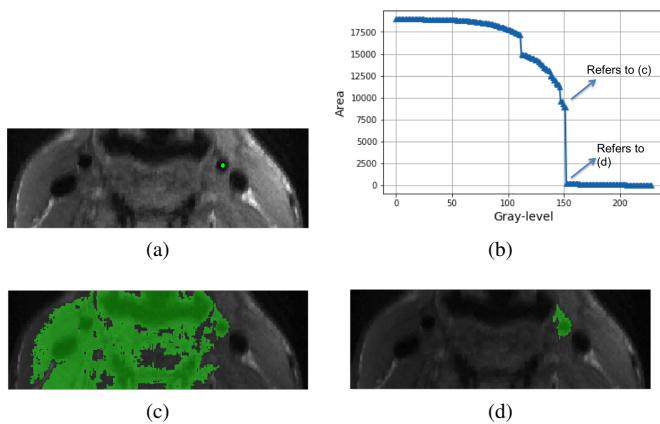

Fig. 3. Max-tree area signature analysis: (a) carotid image with seed point highlighted in green. (b) Area signature starting at the node corresponding to the seed. (c) Node reconstruction at gray-level 151. (d) Node reconstruction at gray-level 152.

D. Tie-zone Watershed Transform from Markers

The watershed transform from markers [16] segments the image based on a flooding procedure starting from imposed markers in the image (Figure 4). The excellence of the segmentation results are dependent of the quality of the markers chosen.
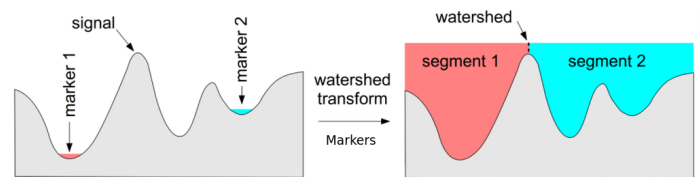

Fig. 4. Watershed from markers operation.

The watershed transform from markers can be seen as an optimization problem. Audigier *et al.* [9], [10] showed that the watershed transform may have multiple solutions, and its output may depend on algorithm implementation details, such as the order the image pixels or pixels neighbors are processed. For instance, the watershed result applied to an image can be different of the watershed result applied to the same image rotated by 90°, which is an undesirable feature. The tie-zone watershed [9], [10] assigns a tie-zone label to the regions that have the same cost to more than one marker. The tie-zones regions then may be addressed in a subsequent post-processing step.

The tie-zone watershed from markers applied to a carotid MR image is illustrated in Figure 5. Two markers are used

in this case, one internal marker in the carotid lumen and one external marker on the carotid wall. In this example, the area of the pixels segmented as lumen corresponds to 63 pixels, while the tie-zone area is of 64 pixels, which shows that the tie-zones have significant influence on the segmentation results.
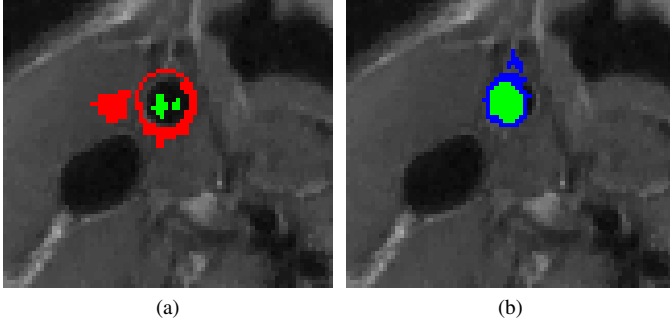

Fig. 5. Illustration of the tie-zone watershed from markers. (a) Internal (green) and external (red) markers. (b) Tie-zone watershed result with the tie-zones shown in blue.

## III. Proposed Methodology

A. Method Assumptions

Our method was developed based on two assumptions with respect to the CCA in adults and a third stipulation with respect to cine FSE imaging. These assumptions are supported theoretically, as well as by typical carotid artery anatomy and our experimental findings. The first assumption is that the diameter of the CCA lumen varies from 4.3 mm to 7.7 mm [17] (Figure 6(a)). The second assumption is that CCA can be modeled as a circle. The third assumption is that two cine FSE images at the same slice position but rebinned at different temporal bins in the cardiac cycle will have similar gray-level intensities. This observation would be theoretically expected based on the implemented reconstruction method [11]–[13] and was experimentally confirmed by histogram analysis (Figure 6(b)).

B. Method Steps

Our solution uses appropriate size and shape information obtained from the max-tree algorithm [8], [18] to find internal and external markers to the carotid artery lumen that are then used by the tie-zone watershed transform. The tie-zones are classified using supervised classification. Our method processes on a slice-by-slice basis, *i.e.*, two-dimensional processing. It has five main steps (Figure 7), which are detailed below.

Step 1: CCA centroid selection: The first step of the method requires the user to select two seed points, one in the left and one in the right carotid artery lumen (Figure 8(a)). These seeds are propagated to the other temporal bins of the acquisition.

Step 2: Internal marker selection: For selecting the internal marker we are interested in the carotid lumen (darkest points of the image), so we build the max-tree of the negative
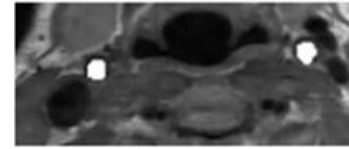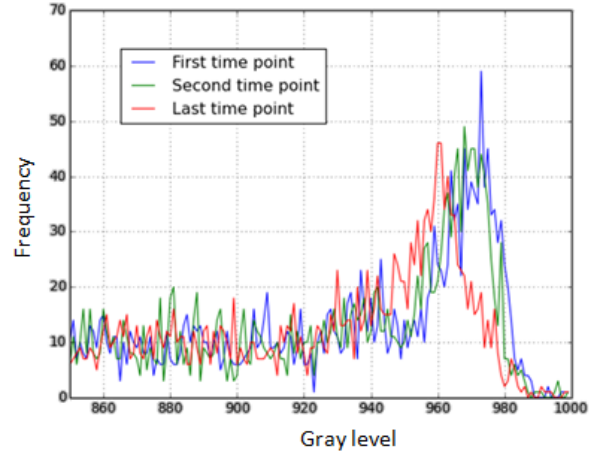
Fig. 6. Key assumptions for post-processing. (a) Manual segmentation of CCA (white). Area of left carotid artery is 25.5 mm^2 and right carotid artery is 31.0 mm^2, which equals an average carotid diameter of 6.3 mm and 5.7 mm, respectively. (b) Intensity histograms from the same slice at different temporal bins are similar (Kolmogorov-Smirnov test found no significant differences between the three histograms, $p = 0.918$).

of the input image. Then, we analyze the max-tree area signature starting from the selected centroid all the way down to the max-tree root. Using *a priori* knowledge of the carotid artery area, we look in the area signature only for structures with an area in the range of 14.5 mm^2 to 46.6 mm^2, because CCA areas are well established from measurements in the literature (diameters ranging from 4.3 mm to 7.7 mm) and we are modeling the vessel cross-section as a circle (with area πr^2), this observation reduces the number of max-tree nodes that need to be analyzed. According our third assumption, the histograms of two consecutive temporal bins are similar, then we select as an internal marker (over the remaining nodes) the candidate with gray-level value closest to the gray level of the previous temporal bin (Figure 8(b)). For the first temporal bin, we select the node with gray level closest to the highest peak of the histogram, once the vessels are the darkest structures of the image.

Step 3: External marker selection: For external markers, we are interested in the vessel wall (brighter structure around the lumen), so we built the max-tree of the gradient image to find nodes around the carotid artery lumen. We use the gradient image, because it accentuates the artery walls due to the sudden change in gray-level between the wall and the lumen. We choose the node in which its centroid has the smallest Euclidean distance compared to the manually selected seed point on Step 1 (Figure 9(a)). Usually, the carotid artery wall
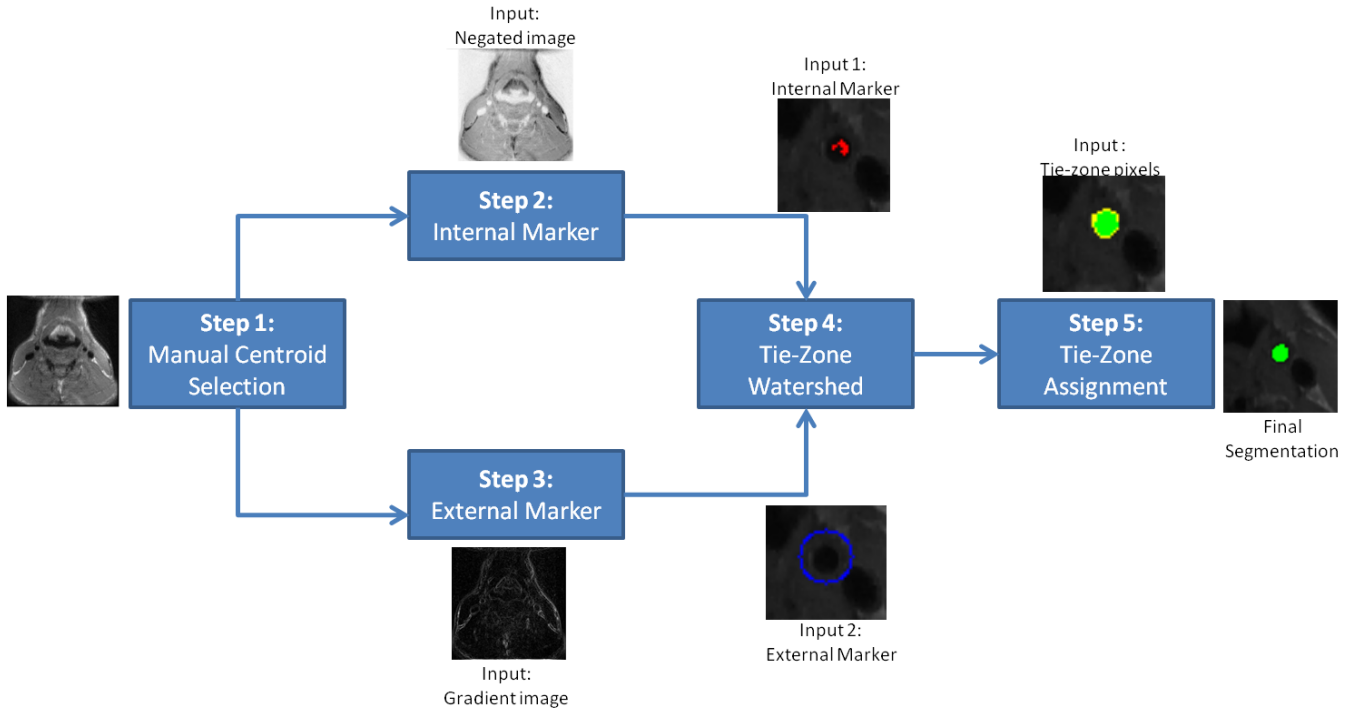
Fig. 7. Flowchart of our proposed method.

is not entirely represented by a single max-tree node (Figure 9(b)), therefore, the final external marker was composed of a circle of diameter equal 1.5 times the greatest distance between the pixels of the selected max-tree node and the manual seed. The diameter is not allowed to exceed 7.7 mm, the assumed maximum diameter for the CCA [17].

Step 4: Tie-zone watershed transform: The tie-zone watershed transform using the selected internal and external markers is applied to the gradient image (Figure 8(c)).

Step 5: Tie-zone assignment: As explained before, the tie-zone watershed returns regions that have the same cost value for both lumen and vessel wall. Those pixels, named here as tie-zone pixels, need to be correctly assigned to improve the method accuracy. The tie-zone pixels are then assigned using a random forest classifier [19] (Figure 8(d)). The classification is performed pixel-by-pixel. The features extracted for each tie-zone pixel are: local binary pattern [20], histogram of oriented gradients computed on the tie-zone image with the bins weighted by the gradient magnitude, and the tie-zone labels histogram. The histograms are computed on a nine-by-nine window centered in the tie-zone pixel (Figure 10). The ground truth used to train the classifier was created using the majority voting consensus of three different manual segmentations made by three different specialists.

C. Experimental Setup

We used forty-five cine FSE datasets acquired on healthy subjects on a 3 T MR scanner (Discovery 750; General Electric, Waukseha, WI) following a protocol approved by our local research ethics board in Calgary. Each dataset had sixteen temporal bins reconstructed across the cardiac cycle. Three manual segmentations were performed independently by three experts on the right CCA. Figure 11 illustrates processing on one example dataset.

A random forest classifier was trained using five randomly selected datasets. In order to get the samples for this classifier, we ran the first four steps of our method. Then, we chose the tie-zone pixels in a way that the number of samples of each class was balanced. The classifier was trained using a cross-validation procedure with the objective of optimizing accuracy. The other forty datasets were used to validate our method.

We assessed our method performance using the Dice coefficient, sensitivity and false positive rate (FPR) metrics. Suppose that G is the "ground truth" image and S is the segmentation we want to assess, the metrics are given by the following equations:

- Dice coefficient:

$$Dice(G, S) = \frac{2|S \cap G|}{|S| + |G|}$$

- Sensitivity:

$$Sensitivity(G, S) = \frac{|G \cap S|}{|G|}$$

- False positive rate:

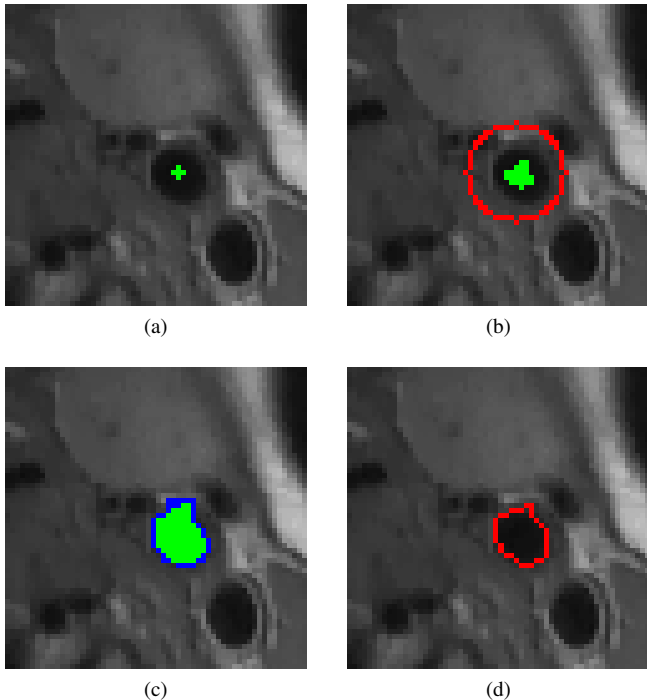$$FPR(G, S) = \frac{|G^c \cap S|}{|G|}$$

Fig. 8. Methodology overview for segementing a left common carotid artery. (a) Manually selected seed (represented here as green cross). (b) Internal (green) and external (red) markers. (c) Tie-zone watershed result (tie-zones in blue). (d) Segmentation result after tie-zone classification (red).
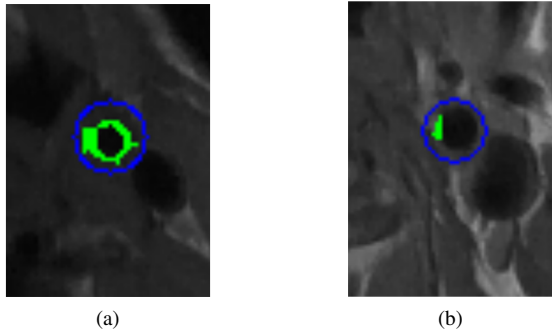

Fig. 9. Example of external markers. (a) In green, node representing the entire vessel wall (smallest Euclidean distance compared to the manually selected seed point). In blue, final external marker (b) In green, case where there is no node representing the entire vessel wall. In blue, final external marker
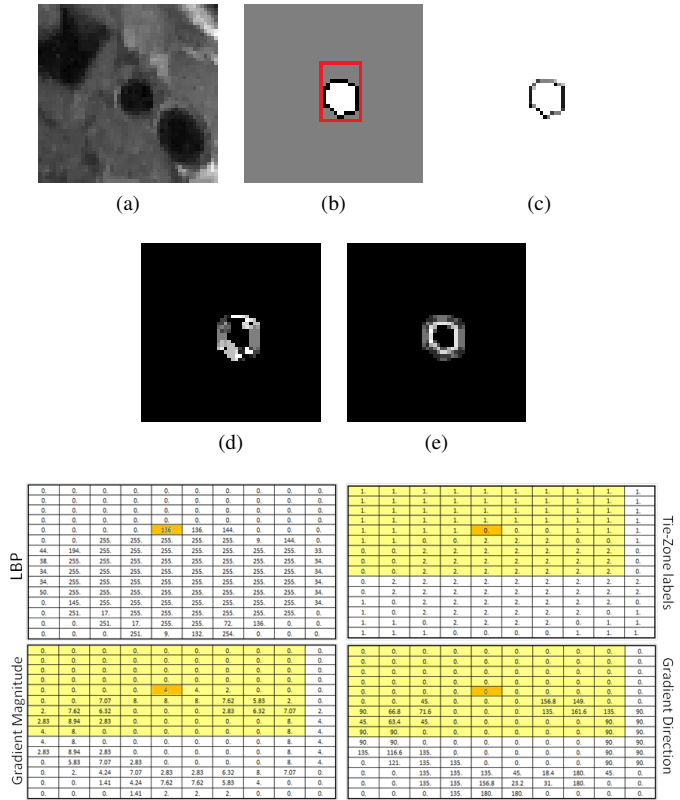

Fig. 10. Overview of our tie-zone classification methodology for carotid artery segmentation. (a) Original Image. (b) Tie-zone watershed transform. White zones are always labeled as lumen, gray zones always labeled as background. The black zone represent the tie-zone pixels. (c) Local Binary pattern image of tie-zone pixels (d) Gradient direction image for tie-zone pixels (e) Gradient magnitude image for tie-zone pixels (f) Feature extraction of the highlighted part of image (b). Each feature vector has 13 components and there is one vector for each tie-zone pixel.

segmented only one CCA.

IV. RESULTS AND DISCUSSION

The five datasets used to train the random forest classifier resulted in a total of $4,762$ samples for training. Its parameters were set using a five-fold cross-validation procedure. The average accuracy obtained was of 0.827 ± 0.006 suggesting room for improvement in the tie-zone classification procedure. Figure 11 provides a comparison between the proposed method and expert segmentation consensus. Good visual agreement was observed. The segmentation results are summarized in Table I.

Our method achieved the best Dice coefficient and FPR metrics and the second best sensitivity result. There are no

The Dice coefficient can be viewed as a compromise between sensitivity and specificity and is probably the most widely used metric to assess segmentation. Sensitivity measures how much brain tissue is included in the segmentation. The FPR gives the fraction of false positive results as a percentage of the ground-truth size. The larger the Dice coefficient and the sensitivity the better is the quality of the segmentation; while the smaller the FPR, the better is the segmentation.

We used the Dice coefficient, sensitivity and FPR to assess the performance of our method. Our method results were compared against the three manual segmentations. The evaluation was only performed for the right carotid, because the experts
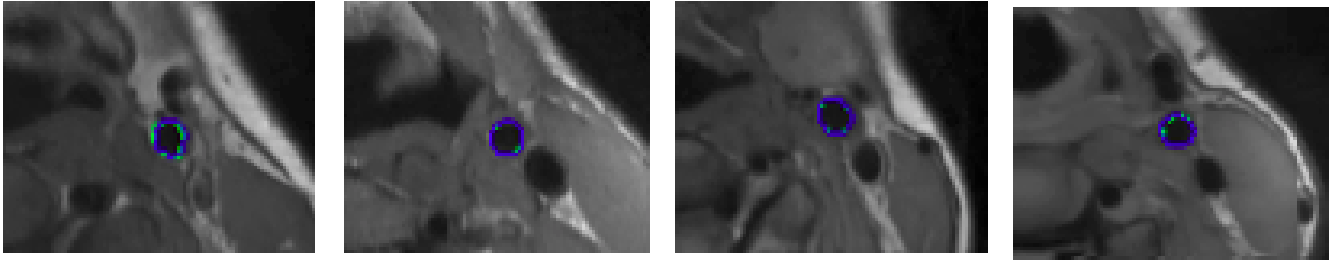
Fig. 11. Representative images from four subjects in the dataset. Our segmentation (blue) is shown overlying the "ground truth" consensus manual segmentation (green). Typically our semi-automated segmentation overlaps the "ground truth" result.

TABLE I
DICE COEFFICIENT, SENSITIVITY AND FALSE POSITIVE RATE (FPR)
METRICS. AVERAGES (MEAN ± STANDARD DEVIATION SHOWN) ACROSS
ALL FORTY SUBJECTS ARE REPORTED COMPARED AGAINST THE MANUAL
SEGMENTATION MAJORITY VOTING CONSENSUS. PERFORMANCE FOR
EACH EXPERT IS ALSO SHOWN.

	Dice	Sensitivity	FPR
Our method	**0.928 ± 0.031**	0.915 ± 0.037	**0.056 ± 0.049**
Expert 1	0.911 ± 0.035	**0.925 ± 0.025**	0.059 ± 0.034
Expert 2	0.907 ± 0.029	0.899 ± 0.044	0.085 ± 0.073
Expert 3	0.912 ± 0.031	0.900 ± 0.043	0.076 ± 0.071

publicly available dynamic carotid segmentation methods to compare against our method. Ukwatta *et al.* [21] tested their method on static MR images also acquired on a 3 T scanner. They achieved a Dice coefficient of 0.93 ± 0.02. Our method achieved a similar average Dice coefficient, but our dataset was more challenging (lower resolution and lower signal-to-noise ratio). As currently implemented, our method tends to underestimate the carotid. With additional refinement, these problems could be fixed by using more accurate markers. Our code is public available at http://miclab.fee.unicamp.br/

V. CONCLUSIONS

This work presented a semi-automatic common carotid artery lumen segmentation method for dynamic MR images. The method was tested on a challenging dataset. Our results are similar to the state-of-the-art segmentation for static MR images [21], which in our opinion are easier to segment due to increased spatial resolution and signal-to-noise ratio. Also, our method compared to the manual segmentation consensus had an agreement close to individual manual segmentation.

The advantage of using dynamic images is that we can analyze artery distensibility. As future work, we intend to make the method fully automated and apply it to artery distensibility analysis. We will also apply it to segmenting more challenging vessel regions, such as the bifurcation, and assess performance in individuals with atherosclerosis. The challenge of making the method fully automatic is that in the same images there may be other vessels similar in size and shape to the carotid. Finally, the challenge of performing distensibility analysis is that the carotid region corresponds to only a small number of pixels within the image, thus few pixels segmented incorrectly will have a significant impact on any resulting distensibility analysis.

REFERENCES

[1] C. Yuan, L. Mitsumori, K. Beach, and K. Maravilla, "Carotid atherosclerotic plaque: Noninvasive mr characterization and identification of vulnerable lesions," *Radiology*, vol. 221, no. 2, pp. 285–299, 2001.

[2] T. Saam, T. Hatsukami, N. Takaya, B. Chu, H. Underhill, W. Kerwin, J.Cai, M. Ferguson, and C. Yuan, "The vulnerable, or high-risk, atherosclerotic plaque: Noninvasive mr imaging for characterization and assessment," *Radiology*, vol. 244, no. 1, pp. 64–77, 2007.

[3] K. Hameeteman, S. Rozie, C. Metz, R. Manniesing, T. van Walsum, A. van der Lugt, W. J. Niessen, and S. Klein, "Automatic carotid artery distensibility measurements from cta using nonrigid registration," *Medical image analysis*, vol. 17, no. 5, pp. 515–524, 2013.

[4] D. Lesage, E. Angelini, I. Bloch, and G. Funka-Lea, "A review of 3d vessel lumen segmentation techniques: Models, features and extraction schemes," *Medical Image Analysis*, vol. 13, no. 6, pp. 819 – 845, 2009, includes Special Section on Computational Biomechanics for Medicine.

[5] A. M. Arias-Lorza, J. Petersen, A. van Engelen, M. Selwaness, A. van der Lugt, W. J. Niessen, and M. de Bruijne, "Carotid artery wall segmentation in multispectral mri by coupled optimal surface graph cuts," *IEEE Transactions on Medical Imaging*, vol. 35, no. 3, pp. 901–911, 2016.

[6] S. S. Kumar and R. Amutha, "Edge detection of angiogram images using the classical image processing techniques," in *Advances in Engineering, Science and Management (ICAESM), 2012 International Conference on*, 2012, pp. 55–60.

[7] A.I.Sakellarios, K. Stefanou, P. Siogkas, V. Tsakanikas, C. Bourantas, L. Athanasiou, T. Exarchos, E. Fotiou, K. Naka, M. Papafaklis, A. Patterson, V. Young, J. Gillard, L. Michalis, and D. Fotiadis, "Novel methodology for 3D reconstruction of carotid arteries and plaque characterization based upon magnetic resonance imaging carotid angiography data," *Magnetic Resonance Imaging*, pp. 1068–82, 2012.

[8] P. Salembier, A. Oliveras, and L. Garrido, "Antiextensive connected operators for image and sequence processing," *IEEE Transactions on Image Processing*, vol. 7, no. 4, pp. 555–570, 1998.

[9] R. Audigier and R. Lotufo, "Tie-zone watershed, bottlenecks, and segmentation robustness analysis." in *SIBGRAPI*. IEEE Computer Society, 2005, pp. 55–62.

[10] R. Audigier, R. Lotufo, and M. Couprie, "The tie-zone watershed: definition, algorithm and applications," in *Image Processing, 2005. ICIP 2005. IEEE International Conference on*, vol. 2, Sept 2005, pp. II–654–7.

[11] J. Mendes, D. Parker, J.Hulet, G. Treiman, and S. Kim, "Cine turbo spin echo imaging," *Magnetic Resonance in Medicine*, vol. 66, no. 5, pp. 1286–1292, 2011.

[12] M. Boesen, L. M. Neto, A. Pulwicki, J. Yerly, M. Lebel, and R., "Fast spin echo imaging of carotid artery dynamics," *Magnetic Resonance in Medicine*, vol. 74, no. 4, pp. 1103–1109, 2015.

[13] M. Lustig, D. Donoho, and J. M. Pauly, "Sparse mri: The application of compressed sensing for rapid mr imaging," *Magnetic Resonance in Medicine*, vol. 58, no. 6, pp. 1182–1195, 2007.

[14] R. Souza, L. Rittner, R. Lotufo, and R. Machado, "An array-based node-oriented max-tree representation," in *2015 IEEE International Conference on Image Processing (ICIP)*, Sept 2015, pp. 3620–3624.

[15] R. Souza, L. Rittner, R. Machado, and R. Lotufo, "Maximal max-tree simplification," in *Pattern Recognition (ICPR), 2014 22nd International Conference on*, Aug 2014, pp. 3132–3137.

[16] R. Lotufo, A. F. ao, and F. Zampirolli, "IFT-watershed from gray-scale marker," *Computer Graphics and Image Processing*, p. 146152, 2002.

[17] Y. Limbu, G. Gurung, R. Malla, R. Rajbhandari, and S. Regmi, "Assessment of carotid artery dimensions by ultrasound in non-smoker healthy adults of both sexes," *Nepal Med Coll*, vol. 8, pp. 200–3, 2006.

[18] R. Jones, "Connected filtering and segmentation using component trees," *Computer Vision and Image Understanding*, vol. 75, no. 3, pp. 215–228, 1999.

[19] L. Breiman, "Random forests," *Mach. Learn.*, vol. 45, no. 1, pp. 5–32, Oct. 2001.

[20] D. He and L. Wang, "Texture unit, texture spectrum, and texture analysis," *Geoscience and Remote Sensing, IEEE Transactions on*, vol. 28, no. 4, pp. 509–512, Jul 1990.

[21] E. Ukwatta, J. Yuan, M. Rajchl, W. Qiu, D. Tessier, and A. Fenster, "3-D carotid multi-region MRI segmentation by globally optimal evolution of coupled surfaces," *IEEE Transactions on Medical Imaging*, vol. 32, pp. 770–785, 2013.